ACS Catalysis

Research Article

pubs.acs.org/acscatalysis

Enhanced Stability of Pd/ZnO Catalyst for CO Oxidative Coupling to Dimethyl Oxalate: Effect of Mg^{2+} Doping

Si-Yan Peng,[†,‡] Zhong-Ning Xu,*[,†,‡] Qing-Song Chen,[†] Zhi-Qiao Wang,[†] Dong-Mei Lv,[†] Jing Sun,[†] Yumin Chen,[†] and Guo-Cong Guo*[,†]

[†]State Key Laboratory of Structural Chemistry, Fujian Institute of Research on the Structure of Matter, Chinese Academy of Sciences, Fuzhou, Fujian 350002, People's Republic of China

[‡]Key Laboratory of Coal to Ethylene Glycol and Its Related Technology, Chinese Academy of Sciences, Fuzhou, Fujian 350002, People's Republic of China

Supporting Information

ABSTRACT: The catalytic performances of supported Pd nanoparticles (NPs) are strongly dependent on the support materials for CO oxidative coupling to dimethyl oxalate (DMO). Herein, hierarchical flower-like ZnO microspheres composed of porous nanosheets are employed as a new support material for a Pd catalyst, which exhibits excellent catalytic activity for CO oxidative coupling to DMO. The conversion of CO and the selectivity to DMO reach up to 67% and 98% at 130 °C, respectively. Unfortunately, the high activity of Pd/ZnO catalyst gradually deteriorates within 100 h. To resolve the poor stability, we further introduce Mg^{2+} ions into the ZnO support. It is exciting that the catalytic activity of the Mg^{2+}-doped-ZnO-supported Pd nanocatalyst (Pd/Mg−ZnO) can be maintained for at least 100 h without obvious decay. Catalytic stability is greatly improved by the doping of Mg^{2+} ions. XRD, UV−visible diffuse reflectance spectra, and high-angle annular dark field scanning transmission electron microscopy characterizations demonstrate that a small portion of Mg^{2+} ions are successfully incorporated into the lattice of the ZnO support to form a Zn−Mg oxide solid solution. XPS, in situ diffuse reflectance Fourier transform infrared spectroscopy, and H_2-temperature-programmed reduction results reveal that the introduction of Mg^{2+} ions into the ZnO support leads to a strong metal−support interaction caused by electron transfer from the ZnO substrate to the Pd NPs, which can effectively restrain the sintering of the active Pd NPs; retard the growth of Pd NPs; and thus, enhance the catalytic stability.

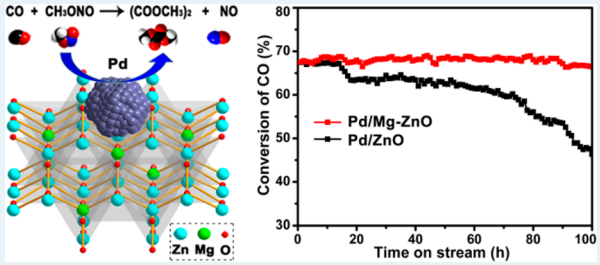

KEYWORDS: *Mg^{2+} doping, Pd/ZnO, coal to ethylene glycol (CTEG), CO oxidative coupling, dimethyl oxalate*

1. INTRODUCTION

Dimethyl oxalate (DMO) is an important chemical product and serves as feedstock for the syntheses of oxalic acid, oxamide, dyes, pharmaceuticals, etc.[1] More importantly, hydrogenation of DMO has also been widely used to synthesize ethylene glycol (EG).[2−7] The traditional method for EG production is based on ethylene oxide hydrolysis.[8] The dwindling sources of petroleum and relatively abundant energy reserve of coal have led to intensive research and development efforts for a new EG synthesis technology called coal to ethylene glycol (CTEG) (Figure S1 in the Supporting Information).[9,10] CTEG has been attracting extensive attention primarily because of its green and atomic economy. CO oxidative coupling to DMO is the crucial step to realize the conversion of inorganic C1 to organic C2 in CTEG.[11]

Pd/α-Al_2O_3 has been widely considered to be an active catalyst for CO oxidative coupling to DMO.[12−17] However, highly efficient Pd-based catalysts supported on other supports are rather limited. The catalytic activity for CO oxidative coupling to DMO has been demonstrated to be strongly dependent on the support materials;[18,19] hence, it is quite essential to develop new support materials for Pd-based catalysts with high performance for CO oxidative coupling to DMO.

ZnO is a direct wide-band-gap (3.37 eV) semiconducting material with a large excitonic binding energy (60 meV) at room temperature.[20] Because of its unique properties, ZnO has been widely used for photocatalysts,[20,21] gas sensors,[22,23] nanolasers,[24,25] solar cells,[26,27] and so on. To meet the demand for diverse applications, ZnO materials with different morphologies, such as one-dimensional (1D) nanowires,[25] nanobelts,[28] nanorods,[22] nanotubes,[29] two-dimensional (2D) nanoplates,[21] and three-dimensional (3D) architectures,[30] have been successfully fabricated over recent decades. In particularly, 3D hierarchical ZnO architectures have received increasing research interest because of their novel properties and superior performances in the fields of photocatalysis,[31] gas sensing,[32] Li ion batteries,[33] and dye-sensitized solar cells.[27] However, few

Received: February 18, 2015
Revised: June 3, 2015
Published: June 8, 2015

DOI: 10.1021/acscatal.5b00365
ACS Catal. 2015, 5, 4410−4417

reports have appeared on the application of 3D porous ZnO architectures as a heterogeneous catalyst support.

In this work, we employ the 3D porous flower-like ZnO as a support for a Pd-based heterogeneous catalyst. It is interesting that the porous ZnO-supported Pd catalyst shows excellent catalytic activity for CO oxidative coupling to DMO. Unfortunately, the high activity of the Pd/ZnO catalyst gradually deteriorates within 100 h and may even deactivate after a longer test.

Because of the high surface energy of nanoparticles (NPs), the sintering of the active metal NPs tends to form larger particles during the process of long-term stability evaluation.[34,35] Notably, the growth of metal NPs, resulting in the loss of active surface area, is a major cause of deactivation for many supported nanocatalysts.[36−38] Thus, considerable efforts have been dedicated to the study of mitigating particle growth using various strategies, including the adoption of different preparation methods,[6,39] the introduction of a second metal to form an intermetallic or alloy,[4,40,41] the addition of a metal or oxide as a structure promoter,[5,42,43] etc. However, limited reports have been focused on retarding the growth of NPs and improving the stability of heterogeneous catalyst by the doping of a foreign element into the support lattice.

In our previous research, we discovered that basic MgO can serve as an excellent support for a Pd catalyst with high stability for CO oxidative coupling to DMO.[19] Moreover, Mg^{2+} and Zn^{2+} have the same valence state and a similar ionic radius.[44] Inspired by these factors, we further introduce Mg^{2+} ions into the ZnO support by a facile solvothermal method. It is exciting that the doping of Mg^{2+} ions can give rise to a significantly enhanced catalytic stability of the Pd/ZnO catalyst. A series of characterization results demonstrate that a small portion of the Mg^{2+} ions are successfully incorporated into the lattice of the ZnO support, which has a positive influence on enhancing the metal−support interaction and mitigating the growth of active Pd NPs. To the best of our knowledge, to date, such Mg^{2+}-doped-ZnO-supported Pd nanocatalysts for CO oxidative coupling to DMO have not been reported.

2. EXPERIMENTAL SECTION

2.1. Catalyst Preparation. *Materials.* K_2PdCl_4 (AR; Sino-Platinum Co., Ltd., China); $CO(NH_2)_2$, $Zn(NO_3)_2{\cdot}6H_2O$, $Mg(NO_3)_2{\cdot}6H_2O$ (AR; Sino-Pharm Chemical Reagent Co., Ltd., China); polyvinylpyrrolidone (PVP; M_w: 40 000; Tokyo Chemical Industry Co., Ltd., Japan); ultrapure water (18 MΩ·cm) were used throughout the experiments. All chemicals were used as received without further purification.

Preparation of ZnO Support. The ZnO support was prepared by a solvothermal method. $Zn(NO_3)_2{\cdot}6H_2O$ (5 mmol; 1.488 g), $CO(NH_2)_2$ (10 mmol; 0.600 g), and PVP (1.665 g) were dissolved in 70 mL of ultrapure water under stirring to form a clear solution. The solution was then transferred to a 100 mL Teflon-lined steel autoclave and maintained at 150 °C for 10 h. After cooling the mixture to room temperature, the precipitate was centrifuged and washed with ultrapure water several times and then dried at 80 °C for 10 h under vacuum. Finally, the hierarchical flower-like ZnO microspheres were obtained by subsequent calcination of the sample at 500 °C in a muffle furnace for 4 h.

Preparation of Mg^{2+}-Doped ZnO Support. Mg^{2+}-doped ZnO (denoted as Mg−ZnO) support was prepared by the same procedure as ZnO, except that the amount of $Zn(NO_3)_2{\cdot}6H_2O$ was changed to 4.5 mmol, and 0.5 mmol of $Mg(NO_3)_2{\cdot}6H_2O$ (0.128 g) was added to the clear solution.

Preparation of Pd/ZnO Catalyst. The Pd/ZnO catalyst was prepared by a wet impregnation method: 16.3 mg of K_2PdCl_4 was dissolved in 15 mL of ultrapure water to form a yellow solution, and then 1.06 g of ZnO support prepared as above was dispersed into the solution with vigorous magnetic stirring at room temperature for 18 h. The solid product was centrifuged and dried at 80 °C for 8 h under vacuum. The dried sample was calcined at 400 °C for 4 h. Finally, the calcined sample was reduced in a hydrogen atmosphere at 300 °C for 3 h. The theoretical Pd loading of the catalyst is 0.5 wt %.

Preparation of Pd/Mg−ZnO Catalyst. Pd/Mg−ZnO catalyst was prepared by the same procedure as the Pd/ZnO catalyst, except that a Mg−ZnO support was used instead of ZnO.

2.2. Catalyst Characterization. Powder X-ray diffraction (XRD) patterns were measured on a glass wafer by a Rigaku MiniFlex 600 diffractometer with a Cu Kα X-ray source (λ = 1.5406 Å) in the range of 25−85° (2θ). The lattice parameters of the samples were calculated by a least-squares method employing the Rietica Rietveld program, in which nickel powder serves as an internal standard for peak position calibration. UV−visible diffuse reflectance spectra (UV−DRS) were measured on a PerkinElmer Lambda 950 spectrophotometer equipped with a diffuse reflectance accessory, and the spectra were recorded in the range of 300−600 nm using $BaSO_4$ as the reference sample.

The BET surface area and pore volume of the different samples were determined by N_2 adsorption−desorption at liquid nitrogen temperature (77 K), which was performed on a Micromeritics ASAP 2020. Thermogravimetric analysis (TGA) experiments were performed on a Mettler Toledo STAR SYSTEM in N_2 with the sample heated in an Al_2O_3 crucible at a heating rate of 10 °C/min. The morphologies of the samples were observed by scanning electron microscopy (SEM, JEOL JSM-6700F).

Transmission electron microscopy (TEM), high-resolution TEM (HRTEM), energy dispersive X-ray spectroscopy (EDS) analysis, high angle annular dark field scanning transmission electron microscopy (HAADF-STEM) and HAADF-STEM-EDS mapping were performed on a Tecnai G^2 F20 field-emission transmission electron microscope operating at an acceleration voltage of 200 kV. The samples were prepared by dropping an ethanol dispersion of samples onto carbon-coated copper grids with a pipettor, and the solvent was allowed to evaporate at room temperature. X-ray photoelectron spectroscopy (XPS) measurements were performed with a VG Escalab 250Xi spectrometer equipped with an Al anode (Al Kα = 1486.6 eV). Samples in powder form were pressed into a wafer for analysis.

In situ diffuse reflectance Fourier transform infrared spectroscopy (DR-FTIRS) measurements were performed on a Nicolet 6700 diffuse reflectance infrared spectrometer equipped with a stainless steel in situ IR flow cell. A 45 mg portion of sample was placed into the cell, having been pretreated in He flow for 20 min at 150 °C. After cooling to room temperature, a background spectrum was collected, then the sample was exposed to a flowing 5% CO/He mixture (30 mL/min) for 30 min. Subsequently, the sample was purged with He for 10 min to flush the CO in the gaseous mixture, and the spectrum was collected again.

DOI: 10.1021/acscatal.5b00365
ACS Catal. 2015, 5, 4410−4417

Temperature-programmed reductions (TPR) were carried out using a Micromeritics AutoChem II 2920 equipped with a liquid nitrogen cooling system. Prior to conducting the H_2-TPR experiment, 100 mg of sample placed in a quartz U tube was first heated to 400 °C for 1 h in a flow of Ar (30 mL/min). After cooling to −50 °C, the sample was exposed to a 10% H_2/Ar mixture (30 mL/min) and then heated to 300 °C at a rate of 10 °C/min.

CO pulse chemisorption and temperature-programmed desorption (TPD) of CO_2 experiments were carried out using an Altamira AMI-300 instrument equipped with a thermal conductivity detector. The dispersion and surface area of Pd for catalysts were calculated from the amount of chemisorbed CO. In a typical CO_2-TPD experiment, 100 mg of sample was treated in a flow of He at 600 °C for 1 h to remove the adsorbed impurities. After cooling to 30 °C in a flow of He, the sample was exposed to 10% CO_2/He mixture (30 mL/min) for 2 h, followed by purging with He for 30 min, and then heated to 800 °C by ramping at 10 °C/min under a flow of He.

2.3. Activity Evaluation. The activities of the catalysts for CO oxidative coupling to DMO were carried out in a fixed-bed quartz tubular reactor. The catalysts (200 mg) were placed in the center of the quartz tubular reactor. The reactant gases (28% CO, 20% CH_3ONO, 4% Ar as internal standard, and 48% N_2 as the balance gas) were passed through the reactor at a gas hourly space velocity (GHSV) of 3000 h^{-1}. The catalytic activity tests were performed under atmospheric pressure. The composition of the reactant gases and reaction products was monitored by an online Shimadzu GC-2014 gas chromatograph equipped with a thermal conductivity detector and a flame ionization detector.

The concentration ratio of CO and CH_3ONO in our reactant gases is 1.4:1, whereas the stoichiometry of CO and CH_3ONO in the reaction is 1:1. Therefore, CO is in excess, and the theoretical maximum value of CO conversion is 71.4%.

The conversion of CO, the selectivity to DMO, and the space−time yields (STY) of DMO were calculated using the following formulas:

$$\text{conversion of CO}(\%) = ([\text{CO}]_{in}/[\text{Ar}]_{in} - [\text{CO}]_{out}/[\text{Ar}]_{out})/([\text{CO}]_{in}/[\text{Ar}]_{in}) \times 100\%$$

$$\text{selectivity to DMO}(\%) = (S_{DMO} \times \text{R-F}_{DMO})/(S_{DMO} \times \text{R-F}_{DMO} + S_{DMC} \times \text{R-F}_{DMC}) \times 100\%$$

$$\text{STY of DMO}(\text{g L}^{-1}\text{ h}^{-1}) = \text{conversion of CO} \times \text{selectivity to DMO} \times \text{GHSV of CO} \times 118.09\ \text{g mol}^{-1}/(2 \times 22.4\ \text{L mol}^{-1})$$

where $[\text{Ar}]_{in}$ and $[\text{Ar}]_{out}$ are the concentrations of Ar at the inlet and outlet and $[\text{CO}]_{in}$ and $[\text{CO}]_{out}$ are the concentrations of CO at the inlet and outlet, respectively. S_{DMO} and S_{DMC} are the peak areas of dimethyl oxalate and dimethyl carbonate, R-F_{DMO} and R-F_{DMC} are the relative correction factors of dimethyl oxalate and dimethyl carbonate, respectively.

3. RESULTS AND DISCUSSION

3.1. Catalytic Activity and Stability. Two types of catalysts (denoted as Pd/ZnO and Pd/Mg−ZnO) have been synthesized under the same conditions except that the support of the latter was obtained with the doping of Mg^{2+} ions. The evaluation of catalytic performance was carried out in a homemade catalytic evaluation device. Figure 1 shows the

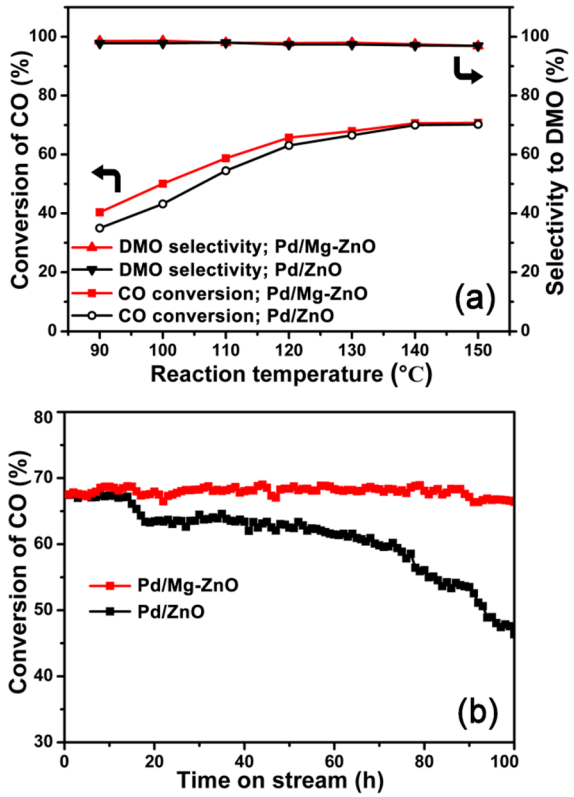

Figure 1. (a) Conversion of CO and selectivity to DMO over Pd/ZnO and Pd/Mg−ZnO catalysts for CO oxidative coupling to DMO at different reaction temperatures. (b) Conversion of CO over Pd/ZnO and Pd/Mg−ZnO catalysts (200 mg) at 130 °C for 100 h.

performances of both catalysts for CO oxidative coupling to DMO. The temperature dependence of conversion of CO (Figure 1a) indicates that catalytic activities of both catalysts increase continually with an increase in the reaction temperature between 90 and 150 °C. The conversion of CO and selectivity to DMO over the Pd/ZnO catalyst unexpectedly reach up to 67% and 98%, respectively, under the same reaction conditions as those for the industrial catalyst (3000 h^{-1} of GHSV, reactants CO/CH_3ONO volume ratio 1.4, 0.1 MPa, 130 °C). The performances of Pd/ZnO catalyst are far superior to the level of industrial catalyst (conversion of CO (34%) and selectivity to DMO (95%)) and even higher than those of other reported Pd/MgO and Pd/α-Al_2O_3 catalysts (Table S1). Moreover, the Pd loading of the Pd/ZnO catalyst is 0.5 wt %, which is only a quarter that of the industrial catalyst (2%). In addition, CO conversion of Pd/ZnO catalyst can reach up to 70% at 140 °C, close to the theoretical maximum value 71.4%, implying that methyl nitrite was consumed nearly completely, which can be verified by the gas chromatogram (Figure S2). Meanwhile, the selectivity to DMO over Pd/ZnO catalyst is always close to 98% in the range 90−150 °C. Unfortunately, the high activity of the Pd/ZnO catalyst gradually deteriorates, with a large decrease of 30% after 100 h (Figure 1b), and may even deactivate after a longer test. To resolve the problem of poor stability, we further introduce Mg^{2+} ions into the ZnO

DOI: 10.1021/acscatal.5b00365
ACS Catal. 2015, 5, 4410−4417

support. It is exciting that the catalytic activity of the Pd/Mg−ZnO catalyst can be maintained for at least 100 h without obvious decay. Moreover, the activity of the Pd/Mg−ZnO catalyst is somewhat higher than that of the Pd/ZnO catalyst, especially at the lower reaction temperature. Therefore, the doping of Mg^{2+} ions into ZnO support can effectively improve the stability of Pd/ZnO catalyst for CO oxidative coupling to DMO. To explore the effect of Mg^{2+} doping, we have performed a series of characterization experiments as follows.

3.2. Support Characterization. XRD patterns of Mg−ZnO and ZnO supports are shown in Figure 2. All the peaks of

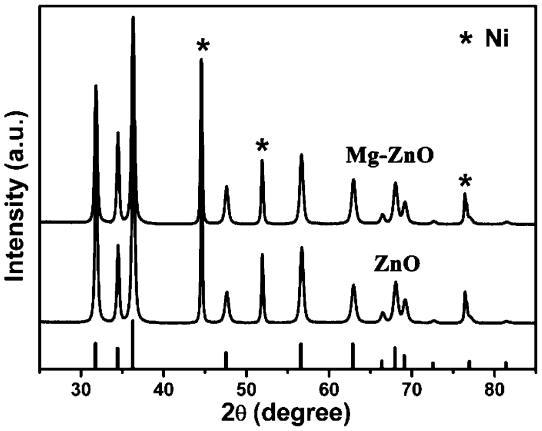

Figure 2. XRD patterns of Mg−ZnO and ZnO supports. Vertical bars at the bottom denote the standard data for a hexagonal wurtzite structure of ZnO (JCPDS, No. 65-3411). Asterisks (*) denote the internal standard of Ni.

both supports match well the standard diffraction data for a hexagonal wurtzite structure of ZnO (JCPDS: No. 65-3411). No diffraction peaks of impurities such as MgO or $Mg(OH)_2$ are observed for Mg−ZnO, which most likely indicates the formation of a Zn−Mg oxide solid solution structure. As seen in Figure S4, the diffraction peaks of the precursors are in good agreement with zinc hydroxide carbonate $[Zn_4CO_3(OH)_6 \cdot H_2O]$ (denoted as ZHC, JCPDS: No. 11-0287).[45] After annealing at 500 °C, the ZHC precursors can transform into a typical wurtzite ZnO structure. Lattice parameters are also examined, as shown in Table 1. It is seen that the *c* and *V* lattice

Table 1. Cell Parameters from Rietveld Analysis for ZnO and Mg−ZnO Supports

supports	*a*, Å	*c*, Å	*c*/*a*	*V*, Å^3
ZnO	3.2499 (1)	5.2088 (2)	1.6028	47.643 (3)
Mg−ZnO	3.2500 (1)	5.2059 (1)	1.6018	47.621 (2)

parameters of Mg−ZnO slightly decrease in comparison with those of ZnO, suggesting a slightly compressed unit cell volume along the *c*-axis orientation caused by the substitution of Zn^{2+} by Mg^{2+}, which is due to a smaller ionic radius (0.57 Å) of Mg^{2+} relative to Zn^{2+} (0.60 Å).[28,46]

UV−DRS investigations were performed for the optical absorption properties of as-prepared supports. Figure 3a presents the UV−DRS profiles of Mg−ZnO and ZnO supports. It is evident that they have similar absorption bands at ∼388 nm, which can be assigned to the optical absorption edge of ZnO; however, the absorption edge of Mg−ZnO shifts toward a lower wavelength relative to ZnO. The Kubelka−Munk

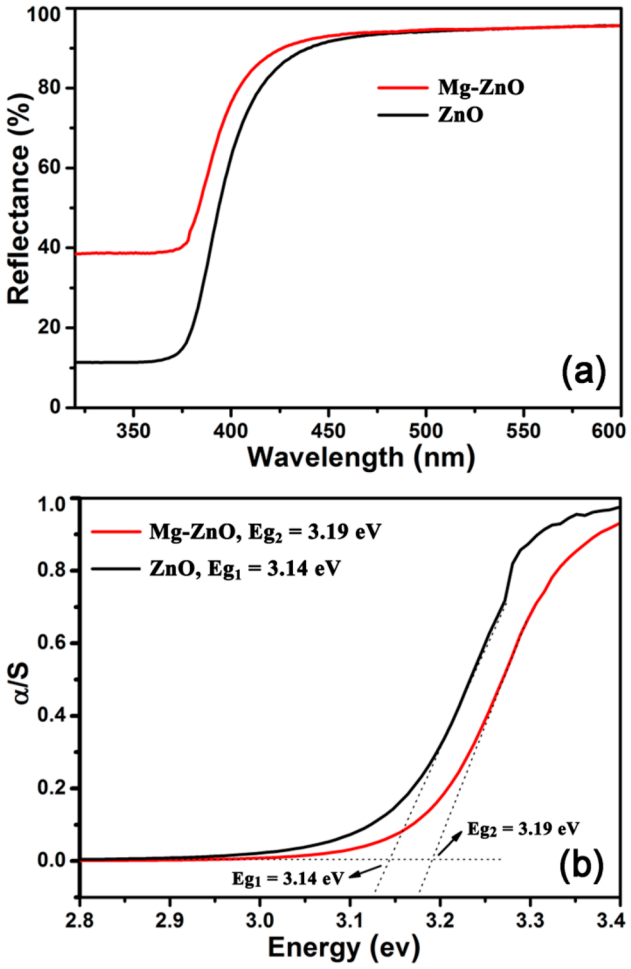

Figure 3. (a) UV−DRS profiles of Mg−ZnO and ZnO supports. (b) Tauc plots constructed from trace "a" according to the Kubelka−Munk function $\alpha/S = (1 - R)^2/2R$; the ordinate values (α/S) have been normalized.

function ($\alpha/S = (1 - R)^2/2R$) is often used to evaluate the band gap of a semiconductor material in terms of the Tauc plot,[47] which is constructed by plotting the Kubelka−Munk function. As illustrated in Figure 3b, the band gap energy increases slightly from 3.14 to 3.19 eV along with the doping of Mg^{2+} ions. The observation of the blue shift in the band gap energy indicates that Mg^{2+} ions are incorporated into the lattice of the ZnO support. This blue shift is probably correlated to the electronic structure modification arising from the substitution of Mg^{2+} for portions of the Zn^{2+} sites in the ZnO crystal.[44]

The morphologies and microstructures of Mg^{2+}-doped samples were investigated by SEM. Figure 4a displays a low magnification SEM image of Mg^{2+}-doped ZHC precursor, indicating that the precursor consists of uniform and well-defined microspheres with an average diameter of 3.7 μm. The enlarged SEM image (Figure 4b) of the precursor suggests that the microspheres are constructed by many interconnected nanosheets as "petals", which are assembled to form a 3D flower-like hierarchical structure. The morphology of the Mg−ZnO support is shown in Figure 4c. It can be seen that the flower-like structure and nanosheets are retained after calcination at 500 °C for 4 h. Nevertheless, it is clear that numerous irregular pores are randomly distributed in the nanosheets (Figure 4d). These pores are caused by the loss of volatile gases, such as H_2O and CO_2, during the thermal

DOI: 10.1021/acscatal.5b00365
ACS Catal. 2015, 5, 4410−4417

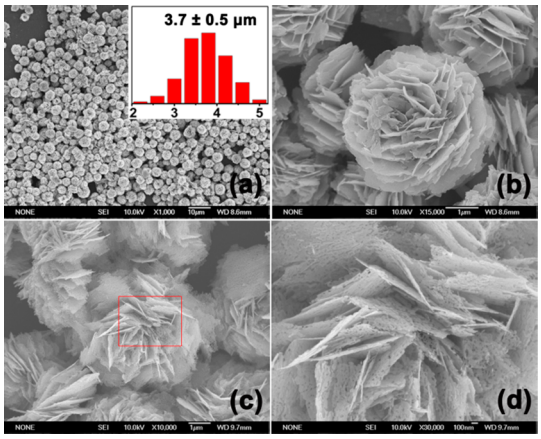

Figure 4. SEM images of (a, b) the Mg^{2+}-doped ZHC precursor and (c, d) the Mg−ZnO support. Panel d represents the enlarged image of the rectangle in panel c.

decomposition of the precursor, which is verified by the TGA curves (Figure S5). The result of the TGA curves indicates that the volatile gases are nearly exhausted at 500 °C, which implies that the precursor can be transformed to Mg−ZnO completely. Figure S6 shows the SEM images of the undoped ZHC precursor and the ZnO support. It is noteworthy that the general morphologies and microstructures of the undoped ZHC precursors and ZnO support are similar to those of the Mg^{2+}-doped samples. Thus, the introduction of Mg^{2+} ions does not cause a significant change in the morphology and microstructure of the ZnO.

The detailed structural characterization of the porous Mg−ZnO was further carried out by HRTEM images and the corresponding selective area electron diffraction (SAED) pattern. The HRTEM image in Figure 5a shows two distinct sets of lattice fringes with interplanar spacings of 0.264 and 0.162 nm, which are unambiguously assigned to the (0002) and $(\bar{2}110)$ planes, respectively, of the hexagonal wurtzite ZnO phase.[48] The incorporation of Mg^{2+} does not cause an evident change in the lattice orientation because the Mg^{2+} content is very low and the radii of Zn^{2+} and Mg^{2+} are fairly close. A similar phenomenon was also observed in the Cu^{2+}-doped ZnO nanocrystals.[48] For Mg−ZnO nanocrystals oriented along the $[01\bar{1}2]$ zone axis, the SAED pattern (inset in Figure 5a) exhibits a series of diffraction spots, which can clearly confirm the single-crystalline nature. The corresponding planes of the diffraction points also match well with the HRTEM observations. The successful Mg^{2+} doping in ZnO nanocrystals can be further confirmed by elemental mapping of Zn and Mg, which was obtained by HAADF-STEM-EDS. As shown in Figure 5b, the element Mg is distributed evenly throughout the whole structure of ZnO, confirming that Mg^{2+} ions are successfully introduced into the lattice of ZnO nanocrystals. In addition, the image obtained by HAADF-STEM further clearly reveals the high porous nature of the Mg−ZnO nanocrystals. The EDS analysis in Figure 5c indicates that the as-synthesized Mg−ZnO microspheres are composed of only Mg, Zn, and O elements, whereas the signals for Cu and C are from the substrate. The concentration of Mg in the final Mg−ZnO sample is 0.91 wt %.

3.3. Catalyst Characterization. To investigate the effect of Mg^{2+} doping on the stability of the Pd/ZnO catalyst, TEM characterization was performed. Figure 6a,b displays the TEM images of the fresh Pd/Mg−ZnO and Pd/ZnO catalysts,

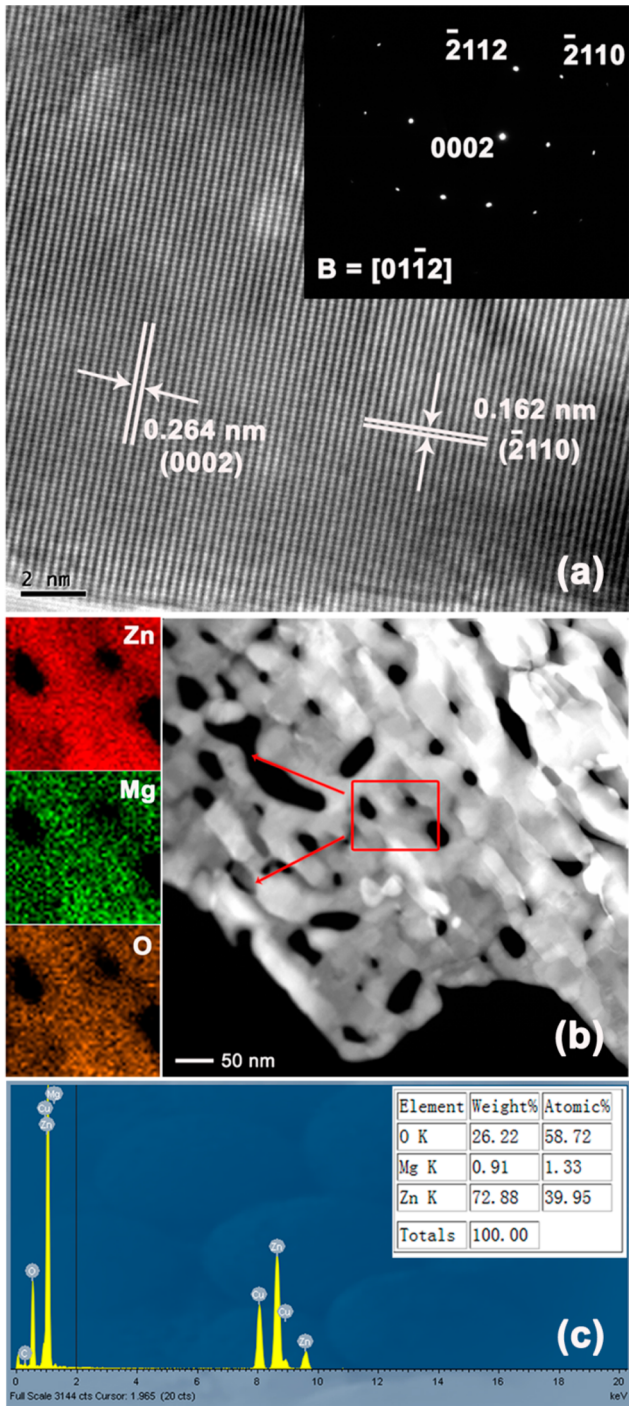

Figure 5. (a) HRTEM image (inset: corresponding SAED pattern), (b) HAADF-STEM-EDS mapping images, and (c) EDS analysis of Mg−ZnO support.

respectively. The active Pd NPs of both catalysts are homogeneously dispersed on the surface of the supports with the same average size and similar size distributions. The particle size distributions show that the mean particle size of both catalysts is ∼2.8 nm. The ultrasmall size, narrow size distributions, and high dispersion are responsible for the high catalytic activities of the both catalysts. The HRTEM image (inset of top left corner in Figure 6a) of the Pd/Mg−ZnO catalyst exhibits well-resolved lattice fringes with a spacing of

DOI: 10.1021/acscatal.5b00365
ACS Catal. 2015, 5, 4410−4417

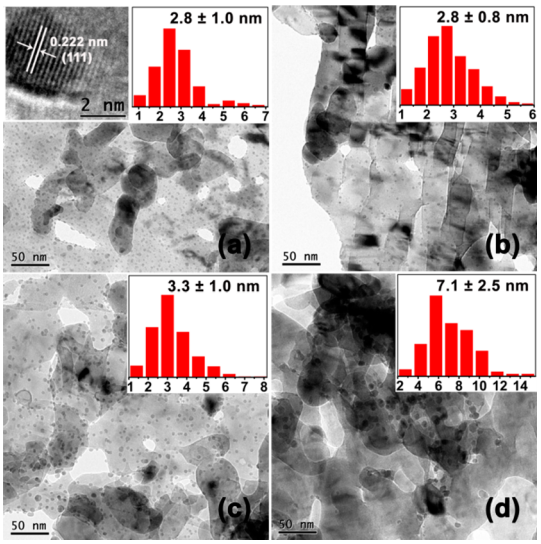

Figure 6. TEM images of the fresh (a) Pd/Mg−ZnO and (b) Pd/ZnO catalysts; the used (c) Pd/Mg−ZnO and (d) Pd/ZnO catalysts after 100 h of evaluation. The insets at top right corners correspond to the size distributions of the Pd NPs.

0.222 nm, corresponding to the interplanar distance of the (111) plane of the face-centered cubic (fcc) Pd.[49]

It is worth noting that the morphology and the high dispersion of the Pd NPs for the used Pd/Mg−ZnO catalyst remain nearly unchanged, and the average size of the Pd NPs increases slightly but negligibly from 2.8 to 3.3 nm after the durability test for 100 h (Figure 6c). These observations can easily account for the high stability of the Pd/Mg−ZnO catalyst, whereas for the used Pd/ZnO catalyst (Figure 6d), the Pd NPs are somewhat aggregated and sintered after 100 h of evaluation, and the average size (7.1 nm) of the Pd NPs becomes much larger than that (2.8 nm) of the fresh one. In addition, the dispersion and surface area of Pd for the fresh and used Pd/Mg−ZnO and Pd/ZnO catalysts were measured by CO pulse chemisorption. It is obvious that the drops in the dispersion and surface area of Pd for Pd/Mg−ZnO after 100 h of evaluation are much less than those for the Pd/ZnO catalyst (Table S3). Thus, the growth of Pd NPs, resulting in the loss of active Pd surface area, is the main reason for the deteriorating activity of the Pd/ZnO catalyst. The introduction of a small portion of Mg^{2+} ions into the ZnO support is beneficial for retarding the growth of the Pd NPs.

Figures S9a, S9b present the XRD patterns of the fresh Pd/Mg−ZnO and Pd/ZnO catalysts, respectively. The sharp diffraction peaks are assigned to the crystalline phase of the ZnO support. No Pd diffraction peak is observed for either of the fresh catalysts, suggesting that the Pd NPs are highly dispersed on the surface of the support. For the used Pd/Mg−ZnO catalyst after 100 h of evaluation, the XRD pattern of Figure S9c shows no significant change compared with the fresh one, but for the used Pd/ZnO catalyst after 100 h evaluation, the XRD pattern of Figure S9d (inset) presents a new weak diffraction peak at 40°, corresponding to the face-centered cubic (fcc) Pd (111) characteristic diffraction. It implies that Pd NPs of the used Pd/Mg−ZnO catalyst are still highly dispersed on the surface of the support during the process of 100 h evaluation, whereas Pd NPs of the used Pd/ZnO catalyst have agglomerated into large NPs. These findings are in agreement with the TEM results. Therefore, on the basis of the characterizations of the TEM, XRD, and catalytic performances, we can demonstrate that the doping of Mg^{2+} ions into the lattice of ZnO can effectively restrain the sintering of Pd NPs, slow down the growth of Pd NPs during the long-term reaction process, and thus further enhance the stability of the Pd/ZnO catalyst for CO oxidative coupling to DMO.

The Pd 3d XPS spectra of Pd/Mg−ZnO and Pd/ZnO catalysts are shown in Figure 7. There are two sets of Pd $3d_{5/2}$ and Pd $3d_{3/2}$ peaks for the Pd/ZnO catalyst after the deconvolution for the XPS profile. The two main peaks appearing at 334.8 and 340.0 eV are assigned to metallic Pd, showing that the oxidation state of the Pd in the Pd/ZnO catalyst is mainly Pd(0) after H_2 reduction. Another two weak peaks centered at 336.4 and 341.6 eV are attributed to Pd(II), indicating that the surfaces of the Pd nanoparticles in the Pd/ZnO catalyst are partially oxidized in air. The situation for the Pd/Mg−ZnO catalyst is similar to that for the Pd/ZnO catalyst. However, it is worth noting that all the binding energies of Pd 3d for the Pd/Mg−ZnO catalyst shift lower by ∼0.4 eV compared with those for the Pd/ZnO catalyst, suggesting electron transfer from the support to the Pd NPs. This interaction in the Pd/Mg−ZnO catalyst can stabilize the Pd NPs and effectively restrain the sintering.

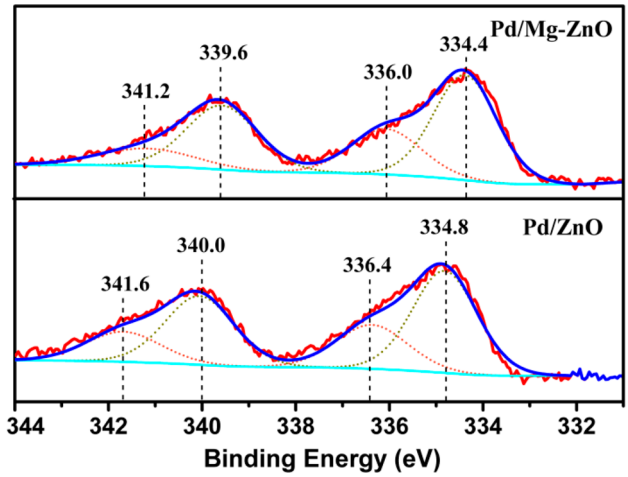

Figure 7. Pd 3d XPS spectra of Pd/Mg−ZnO and Pd/ZnO catalysts.

The electronic interaction between the Pd and the support was further confirmed by the in situ DR-FTIRS study of the CO adsorption, which is often used to probe the surface chemical property of a noble metal on supported catalysts.[50−52] As shown in Figure 8, two absorption bands of CO located at 2091 and 1979 cm^{-1}, which are ascribed to the linearly adsorbed CO and the bridge adsorbed CO on metallic palladium, respectively, appear on the Pd/ZnO catalyst.[12,52,53] It is important to point out that the frequencies of both adsorbed CO in Pd/Mg−ZnO catalyst shift slightly toward to low wavenumber compared to Pd/ZnO catalyst. This slight red shift of CO adsorption frequency is caused by the electron transfer from the support to the Pd NPs. If the electron of the Pd surface is rich,the CO will adsorb at a lower wavenumber, but if the electron of Pd surface is deficient, the CO will adsorb at a higher wavenumber. The electron transfer from the support to the Pd NPs results in the surface of Pd NPs being electron-rich, which would enhance the back-donation from the Pd d band to CO and further increase the CO adsorption energy and weaken the C−O bond.[54]

DOI: 10.1021/acscatal.5b00365
ACS Catal. 2015, 5, 4410−4417

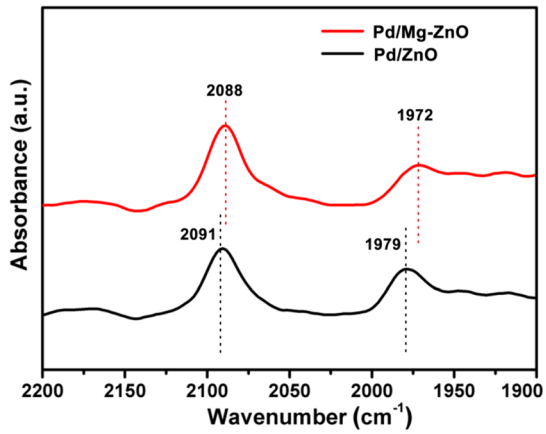

Figure 8. In situ DR-FTIR spectra of adsorbed CO on the Pd/Mg–ZnO and Pd/ZnO catalysts.

H_2-TPR characterizations (Figure S11) were further performed to demonstrate the electron transfer from the support to the Pd NPs. The reduction peak center shifts toward a lower temperature by 5 °C after Mg^{2+} doping, implying that the PdO species in the PdO/Mg–ZnO sample are more easily reduced in comparison with the PdO/ZnO sample, which derives from the relatively lower charge of Pd in the PdO species in the PdO/Mg–ZnO sample as a result of the electron transfer from the support to the PdO species.

To gain more insights into the effect of Mg^{2+} doping, CO_2-TPD experiments were carried out for characterizing the surface basic sites of the catalysts. Under identical experimental conditions, the position of the CO_2 desorption peak reflects the relative strength of the basic sites, and the peak area represents the number of basic sites. As shown in Figure 9, three CO_2

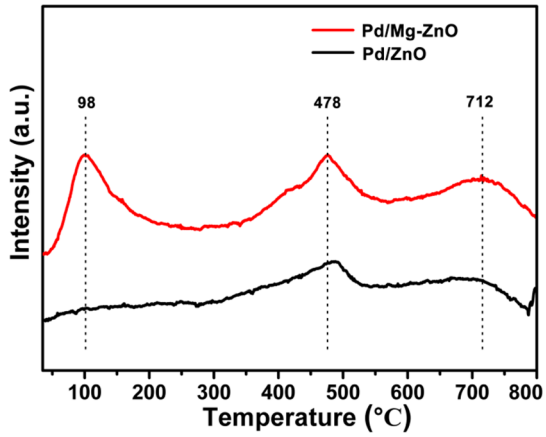

Figure 9. CO_2-TPD profiles of the Pd/Mg–ZnO and Pd/ZnO catalysts.

desorption peaks are observed for the Pd/Mg–ZnO catalyst. The peak at ~98 °C is attributed to the weak basic sites, and the peaks at ~478 and 712 °C correspond to the strong basic sites. It is clear that the intensity of the three peaks is much stronger than that of the Pd/ZnO catalyst, suggesting that Mg^{2+} doping can contribute to creating more basic sites. It is well-known that MgO is a basic support, which contains two types of basic sites. The first is Brønsted basicity, originating from the lattice-bound OH groups, and the other is Lewis basicity, arising from the 3-fold and 4-fold coordinated O^{2-} anions.[55,56] Thus, the introduction of Mg^{2+} ions into the lattice of the ZnO support can improve the number of Lewis basic sites. The electron-rich surface of the Pd NPs in Pd/Mg–ZnO catalyst is probably associated with these Lewis basic sites because they are good electron donors.

4. CONCLUSIONS

In conclusion, we have successfully prepared flower-like ZnO microspheres composed of porous nanosheets using a facile solvothermal method. These hierarchically porous ZnO architectures are employed as a new support material for a Pd catalyst with excellent catalytic activity for CO oxidative coupling to DMO. It is a pity that the high activity of the Pd/ZnO catalyst gradually deteriorates within 100 h because of the growth and sintering of the Pd NPs. To overcome the problem, we introduced Mg^{2+} ions into the ZnO support, and we found that the catalytic stability of Pd/ZnO can be greatly enhanced after Mg^{2+} doping. XRD, UV-DRS, and HAADF-STEM-EDS characterizations demonstrate that Mg^{2+} ions are successfully incorporated into the lattice of the ZnO support. The enhanced stability is mainly attributed to the stabilization of the highly dispersed Pd NPs. The origin of the stabilization effect can be interpreted as the result of the strong electronic interaction between the Pd and the support achieved by the doping of Mg^{2+} ions. This work provides insight that the stability of supported metal catalysts can be improved by the doping of foreign elements into supports.

■ ASSOCIATED CONTENT

Supporting Information

The Supporting Information is available free of charge on the ACS Publications website at DOI: 10.1021/acscatal.5b00365.

Catalytic performances, gas chromatogram of the products, XRD patterns of Mg^{2+}-doped and undoped ZHC precursors, TG curves of Mg^{2+}-doped and undoped ZHC precursors, SEM images, BET surface area and pore volume, dispersion and surface area of Pd, XPS spectra after Ar^+ etching, H_2-TPR profiles (PDF)

■ AUTHOR INFORMATION

Corresponding Authors

*E-mail: znxu@fjirsm.ac.cn.
*E-mail: gcguo@fjirsm.ac.cn.

Notes

The authors declare no competing financial interest.

■ ACKNOWLEDGMENTS

We gratefully acknowledge financial support from the 973 Program (2011CBA00505, 2013CB933200), NSF of China (21403237, 21303202, 21303203), and NSF of Fujian Province (2014J05025).

■ REFERENCES

(1) Zhao, T. J.; Chen, D.; Dai, Y. C.; Yuan, W. K.; Holmen, A. *Ind. Eng. Chem. Res.* **2004**, *43*, 4595–4601.
(2) Yin, A. Y.; Guo, X. Y.; Dai, W. L.; Fan, K. N. *Chem. Commun.* **2010**, *46*, 4348–4350.
(3) Chen, L. F.; Guo, P. J.; Qiao, M. H.; Yan, S. R.; Li, H. X.; Shen, W.; Xu, H. L.; Fan, K. N. *J. Catal.* **2008**, *257*, 172–180.
(4) Huang, Y.; Ariga, H.; Zheng, X. L.; Duan, X. P.; Takakusagi, S.; Asakura, K.; Yuan, Y. Z. *J. Catal.* **2013**, *307*, 74–83.
(5) He, Z.; Lin, H. Q.; He, P.; Yuan, Y. Z. *J. Catal.* **2011**, *277*, 54–63.

DOI: 10.1021/acscatal.5b00365
ACS Catal. 2015, 5, 4410–4417

(6) Zhu, Y. Y.; Wang, S. R.; Zhu, L. J.; Ge, X. L.; Li, X. B.; Luo, Z. Y. *Catal. Lett.* **2010**, *135*, 275−281.
(7) Hu, Q.; Fan, G.; Yang, L.; Li, F. *ChemCatChem* **2014**, *6*, 3501−3510.
(8) Yue, H. R.; Zhao, Y. J.; Ma, X. B.; Gong, J. L. *Chem. Soc. Rev.* **2012**, *41*, 4218−4244.
(9) Zhou, Z. F.; Li, Z. J.; Pan, P. B.; Lin, L.; Qin, Y. Y.; Yao, Y. G. *Huagong Jinzhan* **2010**, *29*, 2003−2009.
(10) Lin, L.; Pan, P. B.; Zhou, Z. F.; Li, Z. J.; Yang, J. X.; Sun, M. L.; Yao, Y. G. *Chin. J. Catal.* **2011**, *32*, 957−969.
(11) Fenton, D. M.; Steinwand, P. J. *J. Org. Chem.* **1974**, *39*, 701−704.
(12) Zhao, X. G.; Lin, Q.; Xiao, W. D. *Appl. Catal., A* **2005**, *284*, 253−257.
(13) Lin, Q.; Ji, Y.; Jiang, Z. D.; Xiao, W. D. *Ind. Eng. Chem. Res.* **2007**, *46*, 7950−7954.
(14) Ji, Y.; Liu, G.; Li, W.; Xiao, W. D. *J. Mol. Catal. A: Chem.* **2009**, *314*, 63−70.
(15) Xu, Z.-N.; Sun, J.; Lin, C.-S.; Jiang, X.-M.; Chen, Q.-S.; Peng, S.-Y.; Wang, M.-S.; Guo, G.-C. *ACS Catal.* **2013**, *3*, 118−122.
(16) Peng, S.-Y.; Xu, Z.-N.; Chen, Q.-S.; Chen, Y.-M.; Sun, J.; Wang, Z.-Q.; Wang, M.-S.; Guo, G.-C. *Chem. Commun.* **2013**, *49*, 5718−5720.
(17) Jin, E. L.; He, L. L.; Zhang, Y. L.; Richard, A. R.; Fan, M. H. *RSC Adv.* **2014**, *4*, 48901−48904.
(18) Uchiumi, S.; Ataka, K.; Matsuzaki, T. *J. Organomet. Chem.* **1999**, *576*, 279−289.
(19) Peng, S.-Y.; Xu, Z.-N.; Chen, Q.-S.; Wang, Z.-Q.; Chen, Y.; Lv, D.-M.; Lu, G.; Guo, G.-C. *Catal. Sci. Technol.* **2014**, *4*, 1925−1930.
(20) Mclaren, A.; Valdes-Solis, T.; Li, G. Q.; Tsang, S. C. *J. Am. Chem. Soc.* **2009**, *131*, 12540−12541.
(21) Hong, Y.; Tian, C. G.; Jiang, B. J.; Wu, A. P.; Zhang, Q.; Tian, G. H.; Fu, H. G. *J. Mater. Chem. A* **2013**, *1*, 5700−5708.
(22) Wang, L. W.; Kang, Y. F.; Liu, X. H.; Zhang, S. M.; Huang, W. P.; Wang, S. R. *Sens. Actuators, B* **2012**, *162*, 237−243.
(23) Hu, P.; Han, N.; Zhang, X.; Yao, M. S.; Cao, Y. B.; Zuo, A.; Yang, G.; Yuan, F. L. *J. Mater. Chem.* **2011**, *21*, 14277−14284.
(24) Huang, M. H.; Mao, S.; Feick, H.; Yan, H. Q.; Wu, Y. Y.; Kind, H.; Weber, E.; Russo, R.; Yang, P. D. *Science* **2001**, *292*, 1897−1899.
(25) Kim, J. Y.; Jeong, H.; Jang, D. J. *J. Nanopart. Res.* **2011**, *13*, 6699−6706.
(26) Lee, Y. J.; Ruby, D. S.; Peters, D. W.; McKenzie, B. B.; Hsu, J. W. P. *Nano Lett.* **2008**, *8*, 1501−1505.
(27) Cheng, C.; Shi, Y. T.; Zhu, C.; Li, W.; Wang, L.; Fung, K. K.; Wang, N. *Phys. Chem. Chem. Phys.* **2011**, *13*, 10631−10634.
(28) Amin, M.; Shah, N. A.; Bhatti, A. S.; Malik, M. A. *CrystEngComm* **2014**, *16*, 6080−6088.
(29) Liu, B.; Zeng, H. C. *Nano Res.* **2009**, *2*, 201−209.
(30) Luo, X. J.; Lou, Z.; Wang, L. L.; Zheng, X. J.; Zhang, T. *New J. Chem.* **2014**, *38*, 84−89.
(31) Zhao, X. H.; Lou, F. J.; Li, M.; Lou, X. D.; Li, Z. Z.; Zhou, J. G. *Ceram. Int.* **2014**, *40*, 5507−5514.
(32) Zhang, H. J.; Wu, R. F.; Chen, Z. W.; Liu, G.; Zhang, Z. N.; Jiao, Z. *CrystEngComm* **2012**, *14*, 1775−1782.
(33) Li, F.; Yang, L. L.; Xu, G.; Huang, X.; Yang, X.; Wei, X.; Ren, Z. H.; Shen, G.; Han, G. R. *J. Alloys Compd.* **2013**, *577*, 663−668.
(34) Benavidez, A. D.; Kovarik, L.; Genc, A.; Agrawal, N.; Larsson, E. M.; Hansen, T. W.; Karim, A. M.; Datye, A. K. *ACS Catal.* **2012**, *2*, 2349−2356.
(35) Hansen, T. W.; DeLaRiva, A. T.; Challa, S. R.; Datye, A. K. *Acc. Chem. Res.* **2013**, *46*, 1720−1730.
(36) Yue, H. R.; Zhao, Y. J.; Zhao, S.; Wang, B.; Ma, X. B.; Gong, J. L. *Nat. Commun.* **2013**, *4*, 2339−2346.
(37) Munnik, P.; Velthoen, M. E. Z.; de Jongh, P. E.; de Jong, K. P.; Gommes, C. J. *Angew. Chem., Int. Ed.* **2014**, *53*, 9493−9497.
(38) Prieto, G.; Zecevic, J.; Friedrich, H.; de Jong, K. P.; de Jongh, P. E. *Nat. Mater.* **2012**, *12*, 34−39.
(39) Zhang, C. X.; Yue, H. R.; Huang, Z. Q.; Li, S. R.; Wu, G. W.; Ma, X. B.; Gong, J. L. *ACS Sustain. Chem. Eng.* **2013**, *1*, 161−173.
(40) Ezekoye, O. K.; Drews, A. R.; Jen, H. W.; Kudla, R. J.; McCabe, R. W.; Sharma, M.; Howe, J. Y.; Allard, L. F.; Graham, G. W.; Pan, X. Q. *J. Catal.* **2011**, *280*, 125−136.
(41) Cao, A.; Veser, G. *Nat. Mater.* **2010**, *9*, 75−81.
(42) Calles, J. A.; Carrero, A.; Vizcaino, A. J.; Garcia-Moreno, L. *Catal. Today* **2014**, *227*, 198−206.
(43) Zhao, S.; Yue, H. R.; Zhao, Y. J.; Wang, B.; Geng, Y. C.; Lv, J.; Wang, S. P.; Gong, J. L.; Ma, X. B. *J. Catal.* **2013**, *297*, 142−150.
(44) Qiu, X.; Li, L.; Zheng, J.; Liu, J.; Sun, X.; Li, G. *J. Phys. Chem. C* **2008**, *112*, 12242−12248.
(45) Zhou, X.; Hu, Z.; Fan, Y.; Chen, S.; Ding, W.; Xu, N. *J. Phys. Chem. C* **2008**, *112*, 11722−11728.
(46) Wang, F. Z.; Zhao, C.; Liu, B.; Yuan, S. C. *J. Phys. D: Appl. Phys.* **2009**, *42*, 115411−115414.
(47) Tauc, J.; Grigorovici, R.; Vancu, A. *Phys. Status Solidi B* **1966**, *15*, 627−637.
(48) Lu, Y. H.; Lin, W. H.; Yang, C. Y.; Chiu, Y. H.; Pu, Y. C.; Lee, M. H.; Tseng, Y. C.; Hsu, Y. J. *Nanoscale* **2014**, *6*, 8796−8803.
(49) Niu, Z. Q.; Zhen, Y. R.; Gong, M.; Peng, Q.; Nordlander, P.; Li, Y. D. *Chem. Sci.* **2011**, *2*, 2392−2395.
(50) Liu, X.; Liu, M. H.; Luo, Y. C.; Mou, C. Y.; Lin, S. D.; Cheng, H.; Chen, J. M.; Lee, J. F.; Lin, T. S. *J. Am. Chem. Soc.* **2012**, *134*, 10251−10258.
(51) Zhang, H.; Sun, J.; Dagle, V. L.; Halevi, B.; Datye, A. K.; Wang, Y. *ACS Catal.* **2014**, *4*, 2379−2386.
(52) Conant, T.; Karim, A. M.; Lebarbier, V.; Wang, Y.; Girgsdies, F.; Schloegl, R.; Datye, A. *J. Catal.* **2008**, *257*, 64−70.
(53) Gao, Z. H.; Liu, Z. C.; He, F.; Xu, G. H. *J. Mol. Catal. A: Chem.* **2005**, *235*, 143−149.
(54) Fottinger, K. *Catal. Today* **2013**, *208*, 106−112.
(55) Liu, Z.; Cortes-Concepcion, J. A.; Mustian, M.; Amiridis, M. D. *Appl. Catal., A* **2006**, *302*, 232−236.
(56) Li, S.; Chen, C. H.; Zhan, E. S.; Liu, S. B.; Shen, W. J. *J. Mol. Catal. A: Chem.* **2009**, *304*, 88−94.

DOI: 10.1021/acscatal.5b00365
ACS Catal. 2015, 5, 4410−4417